CrossMark

REGULAR PAPER

Xin Wen · Yingzheng Liu · Hui Tang

Near-field interaction of an inclined jet with a crossflow: LIF visualization and TR-PIV measurement

Abstract Experiments are conducted in a water tunnel to investigate the near-field interaction of an inclined jet with a crossflow over a flat plate. The tunnel contains a jet emerging from a round pipe inclined at a 30° angle to the streamwise direction of the crossflow. The flow structures induced by the inclined jet are examined with laser-induced fluorescence (LIF) visualization and time-resolved particle image velocimetry (TR-PIV). The behaviors of the near-field flow are compared at four different jet-to-cross-flow velocity ratios (VRs): 0.25, 0.5, 0.75, and 1.0. It is found that the inclined configuration significantly weakens the interaction between the jet and the crossflow, especially at lower VRs. As such, at VR ≤0.5 (typically at VR = 0.25), the inclined jet-in-crossflow (JICF) behaves differently from a highly unsteady normal JICF at low VRs. The flow patterns are relatively simple and only weakly unsteady. A counter-rotating vortex pair (CRVP) is well observed. As VR increases up to 1.0, the inclined JICF fully detaches from the flat plate and shows the classical topology of the normal JICF at high VRs. Both CRVP and shear layer vortices are well captured in this highly unsteady flow regime. The different flow structures together with the interaction between the inclined jet and the crossflow near the jet exit are found to have a strong impact on the distribution of jet-shear layer, jet trajectory, and the jet influence on the crossflow, especially on the near-wall region. Proper orthogonal decomposition is performed on the TR-PIV results to extract the dominant fluctuating modes and reconstruct phase-averaged flow fields. It is found that the highly unsteady flow regime at VR = 1.0 is very unstable, varying between two flow patterns with different fluctuating frequencies at downstream of the jet column. The jet flow near to the exit is also found to be remarkably unsteady due to the interaction between the emerging jet and the crossflow.

Keywords JICF · Flow structures · PIV · LIF · POD

1 Introduction

The jet-in-crossflow (JICF) is of vital importance to fluid mixing and heat transfer in various industrial applications such as plume dispersion and film cooling in gas turbines, and has received widespread attention in fluid-mechanics research (Sinha et al. 1991; Mahesh 2013). Most of previous studies focused on

X. Wen · Y. Liu (✉)
Key Lab of Education Ministry for Power Machinery and Engineering, School of Mechanical Engineering, Shanghai Jiao Tong University, 800 Dongchuan Road, Shanghai 200240, China
E-mail: yzliu@sjtu.edu.cn

X. Wen · Y. Liu
Gas Turbine Research Institute, Shanghai Jiao Tong University, 800 Dongchuan Road, Shanghai 200240, China

H. Tang
Department of Mechanical Engineering, The Hong Kong Polytechnic University, Kowloon, Hong Kong SAR, China

normal JICF. At high velocity ratios (nominally VR >1), four fundamental vortical structures are generally documented (Kelso and Smits 1995; Haven and Kurosaka 1997; Sau and Mahesh 2008; Lim et al. 2001; Fric and Roshko 2006). They are (New et al. 2003): horseshoe vortex that forms upstream of the jet orifice, jet-shear layer vortices formed primarily at the leading edge and lee side of the jet column, tornado-like wakes extending from the wall to the jet, and counter-rotating vortex pair (CRVP). At low VR, however, the unsteady flow structures are different from those at high VR, and the normal JICF is in fact dominantly driven by periodic hairpin vortices (Sau and Mahesh 2008; Mahesh 2013). Bidan and Nikitopoulos (2013) identified attached and detached normal JICF regimes at VR <0.275 and VR >0.6, respectively. The latter exhibited classic vortical structures observed at high VRs, whereas the former exhibited four dominant ones: hairpin vortices, quasi-streamwise side vortices, horseshoe vortex, and inner vortex. Similarly, Cambonie and Aider (2014) provided a complete transition of JICF regime from a very low VR to high ones ranged between 0.16 and 2.13. Using rounded transition values, they summarized as that: the jet is almost attached and strongly interacts with the boundary layer when VR <0.6, hairpin vortices and horseshoe vortex are observed as major vortical structures in this regime; the jet detached from the wall when VR >0.6; at VR >1.25, the classical JICF regime recovers. It is worth noting that most of the previous studies showed that the normal JICF is highly unsteady and is easily periodically swept by the crossflow at VR <0.5.

Compared to normal JICF, the jet issued into the crossflow through a hole with a streamwise inclination (termed inclined JICF) is much less studied, which, however, is a widely used method for film cooling. Because this film-cooling method is not perfectly designed for the near-hole region (Sinha et al. 1991), the near field of the inclined JICF shows complicated, highly unsteady three-dimensional behavior; this is closely associated with the sudden decrease in film-cooling effectiveness immediately behind the jet orifice, typically resulting in local overheating and damage to the blade (Kohli and Bogard 1998). Therefore, a deeper understanding of the flow structures in the near field of the inclined JICF is highly desired.

Many studies have sought to use numerical methods to delineate the dynamics of the flow structures buried in the inclined JICF. Foroutan and Yavuzkurt (2015) compared the ability of numerical models to capture the flow structures in the near-field region of a 30° inclined JICF and found considerable discrepancies among them in the near-hole region. Guo et al. (2006) numerically compared the flow structures in a normal and a 30° inclined JICF at the VR range of $0.1 < VR < 0.48$. Compared with normal injection, the forward inclination shifted the CRVP downstream and reduced its strength. In their study, hairpin vortices are not mentioned. Acharya and Leedom (2012) numerically examined the effect of the feeding-pipe length and the jet-incline angle on film cooling. Longer feeding pipes were, in general, beneficial for film cooling, largely because of the resulting flow structures. Kalghatgi and Acharya (2014) then identified the existence of a CRVP, hairpin vortices, shear layer vortices, and a horseshoe vortex in a large downstream region of the jet orifice up to $x = 15D_o$, where D_o is the diameter of the jet pipe. Combining numerical simulations, visualizations using Mie scattering, and measurements using hotwire anemometry, Bidan et al. (2012) noted the development of a pair of longitudinal streamwise vortices on the sides of the hairpin vortices in a large region of an inclined JICF, up to $x = 12D_o$. In a numerical study, Sakai et al. (2014) found that the vortical flow structures changed significantly with VR in the range of $0.1 < VR < 1.0$: hairpin vortices dominated at lower VRs, whereas pairs of hanging vortices, rear vortices, vertical streaks, and shear layer vortices were formed (in that order) as the VR increased. Using high-speed photography and hotwire anemometry, Fawcett et al. (2013) also found that the dominating flow structures changed from hairpin vortices at lower VRs to shear layer vortices at higher VRs. Dai et al. (2016) conducted experimental visualizations using laser-induced fluorescence (LIF) and measurements using particle image velocimetry (PIV) in a water tunnel to validate their numerical methods. Their simulations demonstrated that the CRVP and the hairpin vortices resulted not only from the cross-flow boundary-layer vortices, but also, or even principally, from the coherent structures induced within a short pipe tube ($L/D_o = 3.8$, where L is the length of the pipe) fed by a plenum chamber. From the range of studies mentioned above, the flow structures of an inclined JICF in the near-field region of the jet orifice are still under debate, and very few experimental attempts have been made to elucidate this important issue.

This study mainly focuses on the flow structures in the near field of a streamwise 30° inclined JICF. The well-documented normal JICF is referred to explain the formation of the flow structures in the current inclined JICF, and more importantly, to identify the difference introduced by the inclined injection. To this end, the inclined JICF in a low-speed recirculation water channel is visualized using LIF and measured using TR-PIV. The spatiotemporal variations of the flow structures and their interaction with the crossflow are examined at low VRs (0.25–1.0). The experimental results are discussed intensively in terms of instantaneous flow visualizations, instantaneous vorticity fields, time-averaged velocity and vorticity fields,

velocity profiles, and jet trajectories extracted from the time-averaged flow fields. The near-wall influence of the flow structures is also examined. The proper orthogonal decomposition (POD) of the spatio-temporally varying velocity fields is performed to extract dominating flow patterns and fluctuation frequency as well as to obtain phase-averaged flow fields.

2 Experimental apparatus

The experiments are performed in a water tunnel with a test section of 1050 mm (L) × 150 mm (W) × 200 mm (H). The schematic drawing of test rig is shown in Fig. 1. To prevent flow separation at the leading edge, the upstream plate was manufactured with a 1:5 elliptical edge. The jet pipe has a diameter of $D_o = 15$ mm and is 400 mm downstream from the plate leading edge with an inclined angle of $\alpha = 30°$ to the flat plate. The area of the effective elliptical exit S is defined as $\pi D_o^2/2$. The jet pipe is especially designed with honeycomb structures and fine screens to avoid the formation of unsteady flow structures inside the long pipe, which has a length-to-diameter ratio of $L/D_o = 13$. The cross-flow speed is fixed at $U_\infty = 0.044$ m/s with a turbulence intensity less than 1.0%. The cross-flow boundary-layer thickness is measured at $3D_o$ downstream from the jet-exit center using PIV technique with no jet flows and is estimated to be $\delta/D_o = 1.5$ when assessed at 95% of the mean cross-flow velocity. While the boundary layer is expected to be laminar, its thickness is larger than what is predicted by Blasius solution and the most likely cause for this discrepancy is the use of an elliptical leading edge during the present study, which could have encouraged boundary-layer growth (New and Zang 2015). Water is channeled from an overhead settling chamber into the jet apparatus driven by gravity, and a flow meter monitors the volume flow rate of the jet with an uncertainty level of 2.5%. The working fluid is water at ambient temperature for both the crossflow and the jet flow, resulting in a density ratio of $\rho_j/\rho_\infty = 1$ and a blowing ratio of $\rho_j U_j/\rho_\infty U_\infty$, which equals a VR of U_j/U_∞. By tuning the flow meter to control the flow rate through the jet pipe Q, four VRs are selected: 0.25, 0.5, 0.75, and 1.0, based on the effective exit area S. The origin of the coordinate system is set at the center of the jet orifice, with the x-axis pointing in the cross-flow direction, the y-axis pointing in the downward wall-normal direction, and the z-axis pointing in the spanwise direction.

LIF is used to visualize the local qualitative flow behavior and prominent vortical structures induced by the inclined jet in the crossflow. As shown in Fig. 2, a 5-W, 532-nm-wavelength diode-pumped solid-state continuous-wave laser provides an approximately 1-mm-thick laser sheet. A fluorescent dye, Rhodamine-B, which had been thoroughly premixed with the jet supply water in the settling chamber, is used to track and visualize the flow structures. A high-speed camera (Mikrotron, MC1362) mounted with a 60-mm lens (Nikon) is used to capture the view of interest ($-2D_o < x < 7D_o$, $0 < y < 3D_o$, $-1.5D_o < z < 1.5D_o$) at 300 Hz. During the experiment, an RAID (redundant arrays of inexpensive disks) system of 16 solid-state disks with a total storage capacity of 1 TB, in combination with two full camera-link interfaces between the high-speed camera and the image adapter card, facilitate the real-time data transfer from the camera to the disks (Liu et al. 2011; Liu and Zhang 2015). A total of 22,200 images of the flow patterns are successively acquired. As shown in Fig. 1b–d, LIF visualization is performed on several selected planes: the mid-span plane (Fig. 1b), the wall-parallel plane with an offset of $0.27D_o$ (4 mm) from the wall (Fig. 1c), and four wall-normal spanwise planes (Fig. 1d).

TR-PIV is used to obtain quantitative information on the flow field with high temporal and spatial resolution. The TR-PIV measurement shares a similar setup with the LIF visualizations, as shown in Fig. 2. To facilitate the PIV measurements, the entire water tunnel is seeded with glass beads ($\rho \approx 1050$ kg/m^3, $d \approx 10$ μm) as tracer particles. The high-speed camera again operates at 300 Hz, which is sufficient to cover the range of frequencies of interest. A PIV software package, Micro-Vec (PIVTec, China), is used to determine the velocity vectors. A multigrid cross-correlation technique (Raffel et al. 2013), in combination with subpixel recognition by Gaussian fitting (Yasuhiko et al. 2000), is applied with a final interrogation window size of 32 × 32 pixels with 50% overlap. A measurement grid of velocity vectors with a spacing of 1.6 mm × 1.6 mm (about 10% of the jet diameter D_o) is then obtained. Due to the strong velocity gradient on the jet-shear layer, more tracking particles are added to the settling chamber to make sure that there are at least ten particles per interrogation windows. As the major source of uncertainty, the root-mean-square fluctuation of the PIV-measured particle displacement is estimated to be about 0.08 pixels in the field images (Willert and Gharib 1991). Therefore, the uncertainties in the measurements determined by recursive image interrogation are approximately 1% in the streamwise and wall-normal velocity components when the particle displacement is about 8 pixels in the interrogation window. A total of 22,199 instantaneous velocity
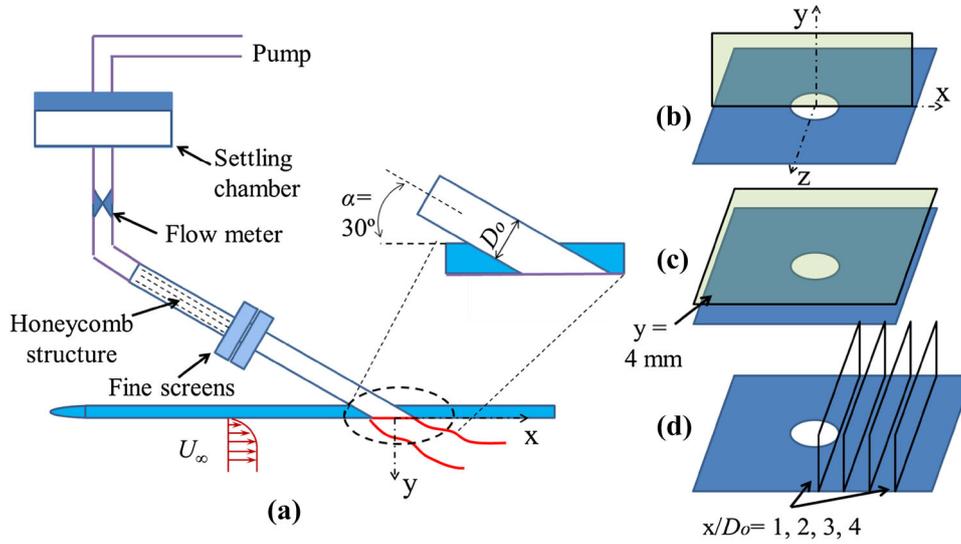
Fig. 1 a Schematic of the test rig, and **b–d** planes for LIF visualization (with *black borders*) and for PIV measurements (*filled in light blue*), not in scale
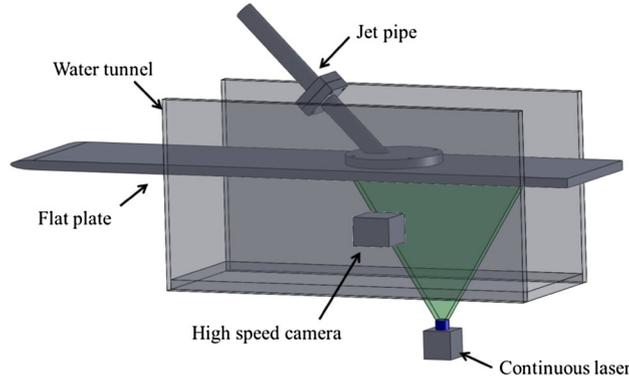
Fig. 2 Setup of LIF visualization and TR-PIV measurements

fields are obtained from the 22,200 sequential images. As shown in Fig. 1b, c, the TR-PIV measurements are performed at two selected planes: the mid-span plane (Fig. 1b) and wall-parallel plane (Fig. 1c).

3 Results and discussion

3.1 LIF visualization

The three-dimensional flow structures in the inclined JICF are presented from the qualitative LIF visualizations in the mid-span plane, the wall-parallel plane, and several wall-normal spanwise planes. At VR = 0.25 and 0.5, the inclined jet is barely detached from the wall and exhibits relatively simple flow structures, as shown in Fig. 3a, b. It is interesting to observe a CRVP under the current low VRs. To show the steadiness of the CRVP, image of the flow-pattern fluctuation on the wall-normal plane $x = 4D_{\mathrm{o}}$ is obtained from 3000 images for 30 s. The fluctuation level on one specific pixel is defined by the root-mean-square deviation from the long-time-averaged value as

$$x_i = \sqrt{\frac{\sum_{n=1}^{N}\left(\hat{x}_i^n - \bar{x}_i\right)^2}{N}} \tag{1}$$

where $\hat{x}_i^n$ is the gray level on the ith pixel of the nth image, $\bar{x}_i$ is the time-averaged value, and $N = 3000$ is the total image used. As shown in Fig. 3c, d, only very weak fluctuation is captured by the bright lines (high fluctuation region), outlining the shape of the CRVP. It is well known that the CRVP persists long after injection and is often found in a time-averaged sense under a relatively high VR (VR >1) in a classical normal JICF (Lim et al. 2001; Fric and Roshko 2006; Mahesh 2013). In a normal JICF and at a high VR $\approx$ 4.6, Lim et al. (2001) identified three distinct folding processes of the shear layer emerging from a nozzle. One process led to the formation of a CRVP on the lateral sides of the jet column, and the other two induced the shear layer vortices on the leading-edge side and lee side of the jet column. Under the current inclination configuration, the first folding process reduces the size of the main jet, as shown in the mid-span plane, while increases the size of the CRVP at both lateral sides, as shown in the wall-normal spanwise planes. In a normal JICF at low VRs (VR <0.5), however, it is well documented that the flow regime is dominated by hairpin vortices that are periodic and highly unstable (Mahesh 2013; Bidan and Nikitopoulos 2013; Cambonie and Aider 2014). Mahesh (2013) has documented that the hairpin vortices form, because the boundary-layer vorticity can overwhelm the leading-edge vorticity in the jet pipe, resulting in vorticity essential being shed from the trailing edge. The vorticity shedding from the trailing edge is generated partly due to the jet-shear layer emerging from the jet and partly due to the interaction of the normal jet injection and the crossflow (Acarlar and Smith 1987; Wen et al. 2015). In the current configuration, the vertical velocity component of the jet flow diminishes due to the inclined jet angle. The interaction between the jet and crossflow is also considerably reduced. As such, hairpin vortices that are resulted from strong interaction between a normal jet and crossflow are not observed in the current inclined JICF which exhibits a weakly unsteady CRVP instead.
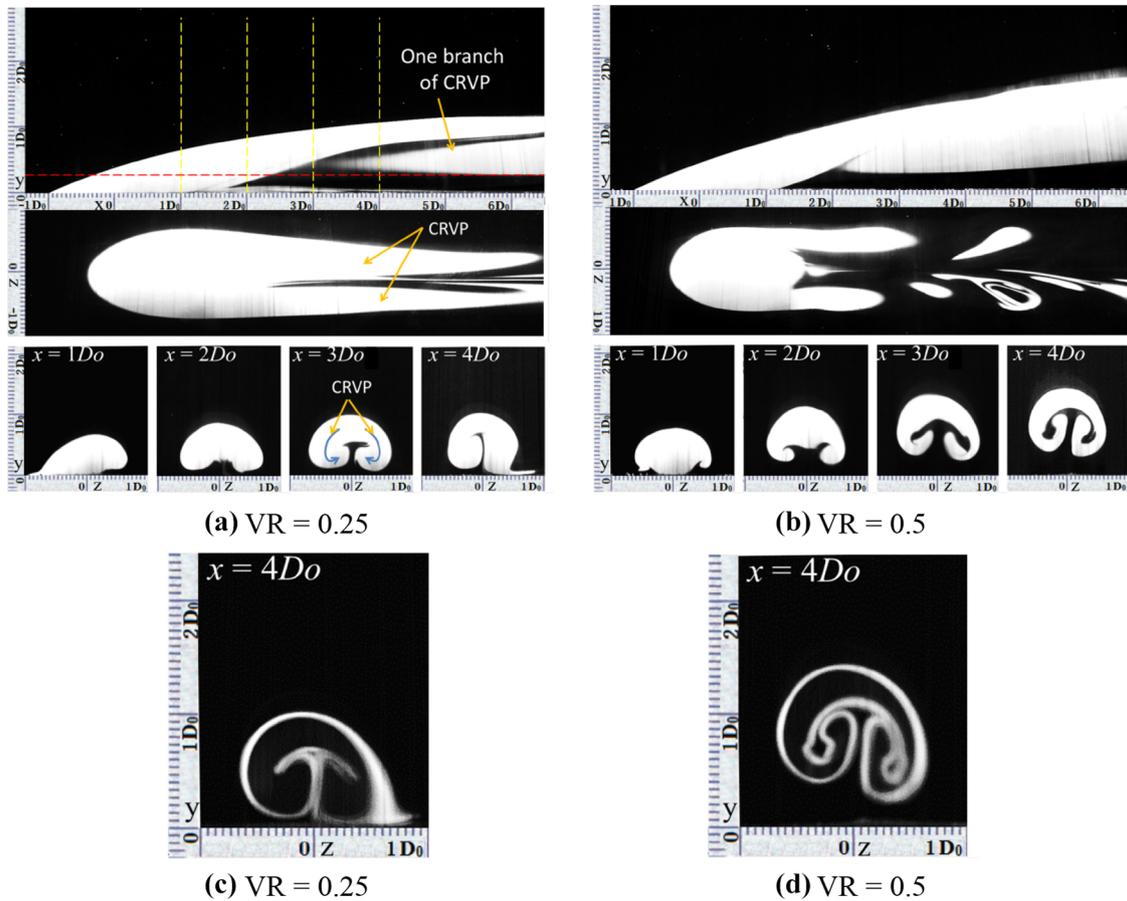
Fig. 3 Instantaneous flow patterns visualized by LIF at **a** VR = 0.25 and **b** 0.5 (*upper row* mid-span plane, *middle row* wall-parallel plane, *lower row* wall-normal spanwise planes). Images of fluctuation level at **c** VR = 0.25 and **d** 0.5. The *red dashed line* indicates the wall-parallel plane, and the *yellow dashed lines* indicate the wall-normal planes

As the VR increases up to 1.0, the flow structures become markedly unsteady, as shown in Fig. 4a, b. The unsteady flow regimes exhibit similar flow patterns to the classical JICF at a high VR. Not only CRVP is observed on lateral sides, but also the jet-shear layer vortices, i.e., leading-edge vortices and lee-side vortices. The Kelvin–Helmholtz instability induces the destabilization of the upstream and downstream shear layers and leads to the formation of periodically shed shear layer vortices on the sides of the jet column. In the current study, at VR = 0.75, a series of lee-side vortices are identified, whereas their counterparts at the leading edge are hardly observed. As VR further increases to 1.0, both leading-edge vortices and lee-side vortices are observed. Although not shown in the current frozen flow patterns, the initiation and formation of these vortices are very unstable both spatially and temporally from long-time observation. In addition, these vortices travel for a short streamwise distance before breaking up into fine-scale structures. Such behaviors are also observed in a classical normal JICF issued from a circular exit with a parabolic exit velocity profile (New et al. 2006). In the current study, the exit velocity profiles have a similar shape to a parabolic line, which will be discussed later in detail. In fact, there is a common difficulty to identify CRVP from the hairpin legs at intermediate VRs (Mahesh 2013). For example, at VR = 0.75 in the current study, the cross section of lee-side vortices is similar to the hairpin heads in the mid-span plane, and the CRVP captured in the spanwise wall-normal planes looks like the flow produced by the hairpin legs. It could be tempting to directly interpret the highly unsteady flow structures as the hairpin vortices usually found in a normal JICF at low VRs (VR <0.5). A few considerations lead us to do so with caution. First, instantaneously, the hairpin legs are discontinuous as revealed in intensive previous studies (Acarlar and Smith 1987; Wen and Tang 2014), whereas CRVP structure, which, although it can be asymmetric in strength with respect to the mid-span plane, has never been documented as discontinuous (Bidan and Nikitopoulos 2013). From the image of fluctuation, as shown in Fig. 4c, although the flow pattern shows a weak fluctuation on the outline, it generally well keeps its shape, indicating that the flow structure is continuous. Furthermore, hairpin vortices are usually found close to the wall and have a remarkable interaction with the boundary layer. In the current study, however, the jet penetrates deeply in the crossflow and detaches from the wall significantly. Therefore, the highly unsteady flow structures at the current flow regime actually exhibits similarly to the classical JICF at high VRs, with CRVP and shear layer vortices are identified. At VR = 1.0 as shown in Fig. 4d, the image shows great fluctuation due to the highly unstable flow structures. The regions of high fluctuation on the lateral sides are believed to be caused by the CRVP, which is also widely observed in time-averaged sense in a normal JICF at high VRs. The horseshoe vortices are not captured, since there is no dye upstream in the current study. The wake vortices may be too weak to be captured.

The weakly unsteady and highly unsteady flow regimes, observed at lower VRs and higher VRs, respectively, will undoubtedly have a significantly different influence on the near field of the inclined JICF. To seek deeper understanding of the flow patterns presented in LIF visualization, quantitative measurements using PIV technique were conducted and the results are discussed below.

3.2 Instantaneous flow patterns

Figure 5 shows a preliminary view of the flow patterns presented by plotting the instantaneous spanwise vorticity fields with the velocity vectors obtained from the PIV measurements in the mid-span plane. In addition, coherent structures are identified using local swirling strength, λ_{ci}, the imaginary part of the complex eigenvalue pair of local velocity gradient (Zhou et al. 1999). An iso-value of $\lambda_{ci} = 0.7$ is used to determine the edge of vortex structures so as to show the shape of vortex structures while filtering out low λ_{ci} value noise. Consistent with the flow visualization results, the flow patterns at lower VRs (VR = 0.25 and 0.5) show weaker unsteadiness than those at higher VRs (VR = 0.75 and 1.0). At VR = 0.25, as shown in Fig. 5a, the shear layer vorticity on the lee side of the jet column is obviously stronger than its counterpart on the leading edge which is hardly observable. As VR increases to 0.5, as shown in Fig. 5b, shear layer vorticity are well captured on both sides, defining the jet column. The shear layer vortices are found to be closer than expectation, indicating that the crossflow has a significant blocking effect on the effective exit area of the inclined jet.

As VR increases to 0.75 and 1.0, the flow regimes become highly unsteady, consisting of series of vortex structures along the jet column. As shown in Fig. 5c at VR = 0.75, the shear layer begins to break and roll up at around $x = 3.5D_o$, generating lee-side vortices. On the other hand, the formation process of the leading-side vortices may be prevented by the closeness of the relative velocities between the jet and the crossflow. As such, the shear layer on the leading edge is weakened to trigger the onset of the Kelvin–

(a) VR = 0.75

(b) VR = 1.0

(c) VR = 0.75

(d) VR = 1.0
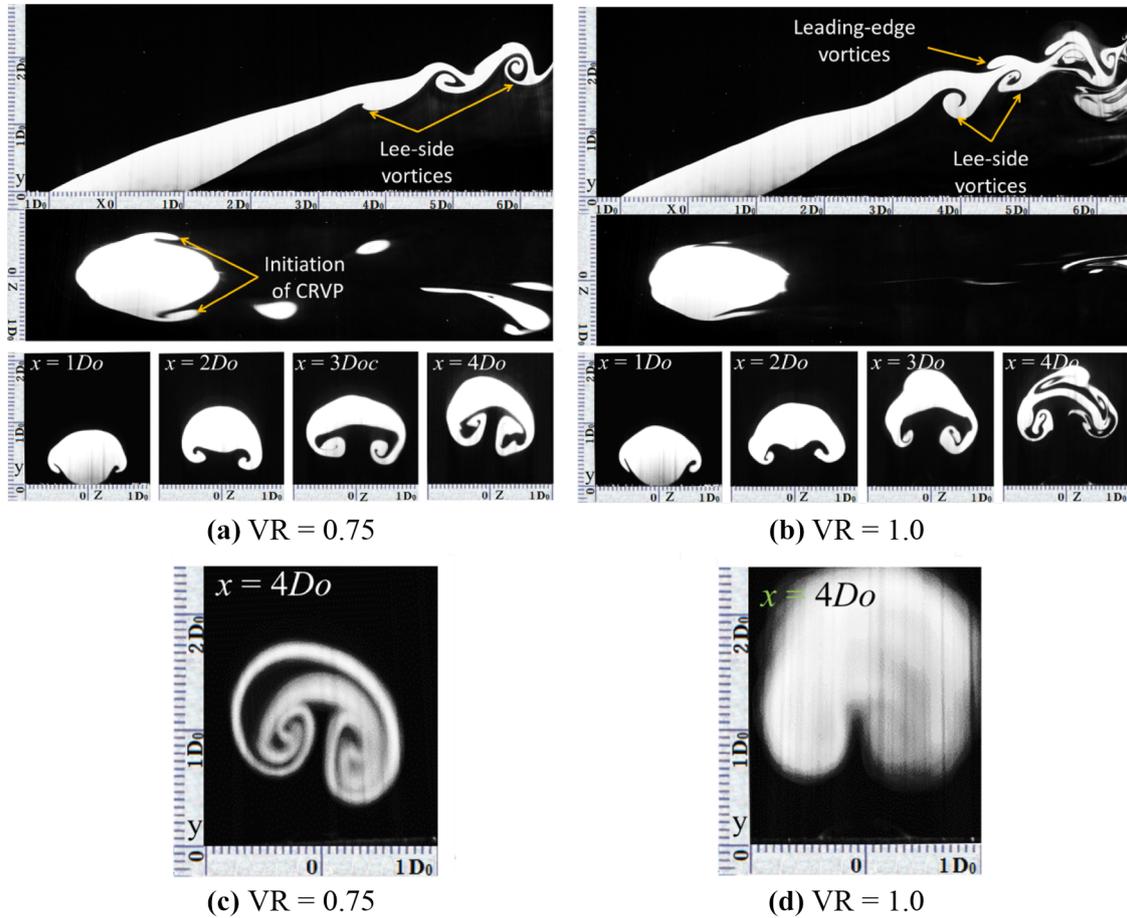
Fig. 4 Instantaneous flow patterns visualized by LIF at **a** VR = 0.75 and **b** 1.0 (*upper row* mid-span plane, *middle row* wall-parallel plane, and *lower row* wall-normal spanwise planes). Images of fluctuation level at **c** VR = 0.75 and **d** 1.0

Helmolt instability. As shown in Fig. 5d, at VR = 1.0, the shear layer breaks and rolls up earlier at around $x = 2.7D_o$, forming both strong leading-edge and lee-side vortices. Due to the formation of such strong vortices, the inclined JICF at higher VRs is believed to have higher entrainment rate than that at lower VRs, which ensures that the cross-flow fluid could be more easily entrained into the jet body. In addition, the jet is strong enough to overcome the blocking effect of the crossflow on the exit, which in return limits the peak jet velocity due to enlarged effective area of jet exit. As a result, the jet penetration height into the crossflow at VR = 0.75 shows no significant difference to that at VR = 0.5. This observation from instantaneous flow patterns will also be confirmed and discussed in detail later based on jet trajectories.

3.3 Time-averaged fields and jet trajectories

Figure 6 presents the time-averaged flow field by plotting the spanwise vorticity and velocity vectors. It can be seen that the shear layer vorticity on the lee-side surpasses that at the leading edge in the full range of the VR. This is shown more clearly in Fig. 7, by plotting the peak vorticity values. This stronger shear layer vorticity on lee side can lead to the stronger vortices at the highly unsteady regimes, as shown in the PLIF visualizations above. As shown by the velocity vectors in Fig. 6, the relatively weak shear layer vorticity on the leading edge is related to the closeness of the relative velocity between the jet flow and crossflow on the leading edge. On the other hand, there is a low-speed region just generated downstream of the jet column due to its blockage effect on the crossflow, resulting in a higher velocity gradient and, therefore, stronger shear layer vorticity on the lee side. The interaction between the jet and crossflow near the exit may also contribute to this difference, which will be discussed later. Besides, as shown in Fig. 7, the peak strength of shear layer vorticty at VR = 0.5 is remarkably higher than expectation, which is even higher than that at
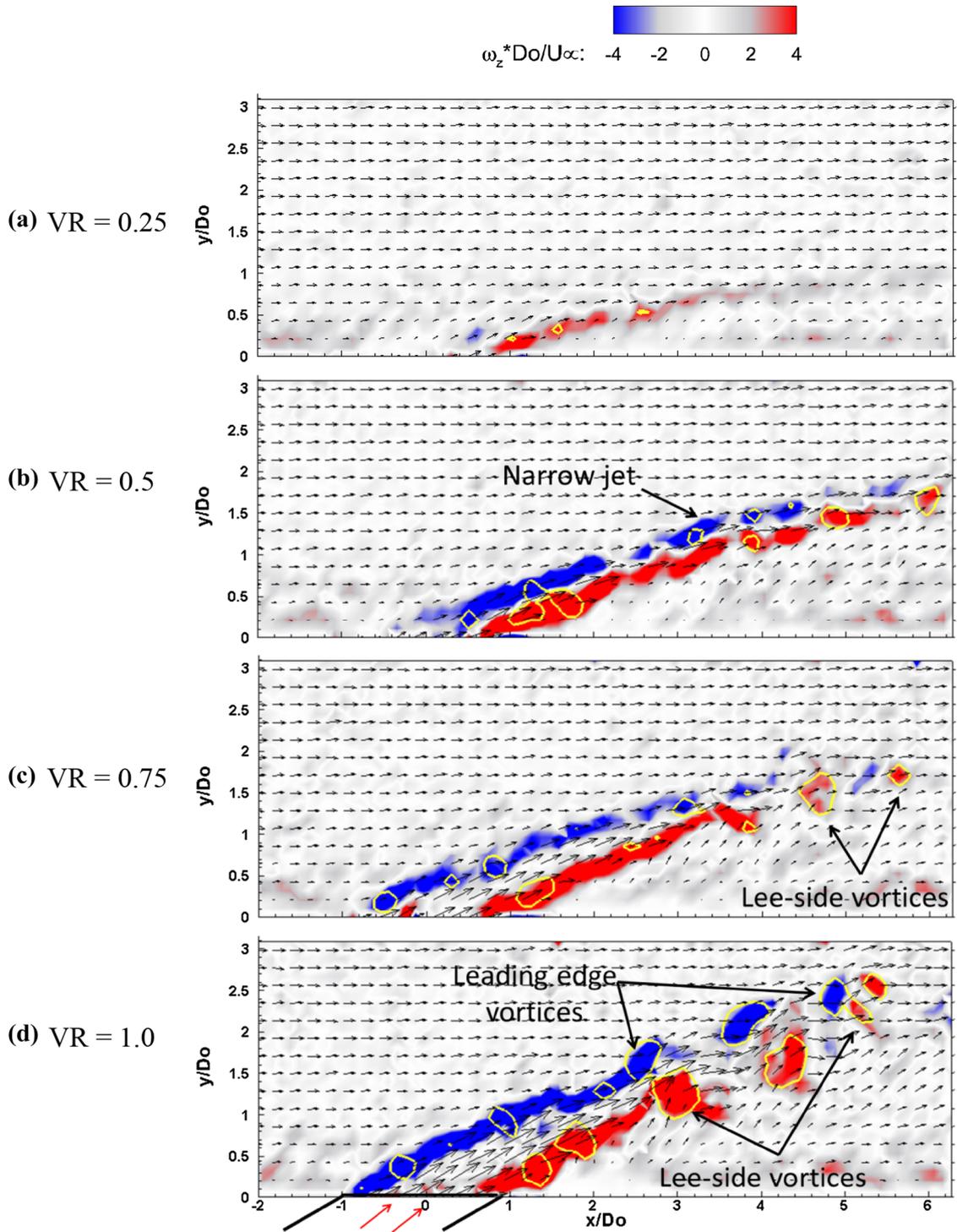
Fig. 5 Contours of instantaneous spanwise vorticity and vortex structures captured by $\lambda_{ci} = 0.7$ (*yellow outlines*) with velocity vectors in the mid-span plane

VR = 1.0. From the turbulent intensity profiles along the vertical line of $x = 5D_o$ in the mid-span plane, as plotted in Fig. 8, it can be seen that the jet at VR = 1.0 induces very strong turbulence along the jet column, indicating the highly unsteady manner and also an intense transfer of momentum and mass between the jet and the crossflow. On the other hand, the weakly unsteady jet only generates very limited fluctuation in the

flow regime. In accordance with the findings from the vorticity fields, it is interesting to find that the jet at VR = 0.5 induces even stronger turbulence than that at VR = 0.75, but with a narrow area. As shown in Fig. 6 at VR = 0.5, the effective jet column is significantly narrowed, which can be directly related to the reduced effective area of the jet exit. Therefore, the time-average speed profiles near the jet exit are examined and compared between two close cases of VR = 0.5 and 0.75. As shown in Fig. 9, the speed profiles near the jet exit in still water are generally close to a parabolic profile. In a normal JICF, it is found that the thicker shear layer associated with a parabolic JICF is able to delay the formation of the leading-edge and lee-side vortices (New et al. 2006), which is also confirmed in the current study by the above LIF visualization and instantaneous PIV measurement. When crossflow is applied, it shifts the location of the peak values of the speed profiles to the lee side of the jet exit at both VRs. As such, a higher velocity gradient is induced on the lee side, whereas lower one on the leading edge. This can also contribute to the stronger shear layer vorticity on the lee side of the jet column. In addition, at VR = 0.5, the crossflow significantly blocks the exit area of the jet flow. Therefore, the speed profile undergoes a "stretching and thinning" process, resulting in a peak speed value that is even higher than VR = 0.75. Within this narrowed jet, stronger shear layer vorticity and turbulence can be induced than expectation.

To appreciate the impact of the different flow patterns on the near field of the JICF, streamwise u and vertical v velocity distributions along the mid-span plane at various x/Do locations are extracted from the time-averaged PIV in two cases of VR = 0.5 and VR = 0.75, as demonstrated in Fig. 10. Figure 11 depicts the time-averaged u and v velocity at VR = 0.5 at various downstream locations from $x/D_o = 0$ to 5. Note that the horizontal axes indicate both the x/D_o locations and the velocity normalized by the cross-flow speed. As shown in Fig. 11a, the emergence of the jet into the crossflow has obviously distorted the boundary-layer velocity profiles along all the examined locations. At $x/D_o = 0$, a velocity minimum is induced at point A which is attributed from the leading-edge shear layer of the jet column. At $x/D_o = 1$, the velocity maxima at point B represents the center of the deflected jet, it is not surprising that it has a higher value that the crossflow. The velocity profiles at $x/D_o = 2$–5 are generally similar to that at $x/D_o = 1$, expect for the upward shift of the peak value location which indicates the jet trajectory. Compared to the velocity profiles of a classical normal JICF which has two velocity maxima points and one minima point (New et al. 2006), there is only one maxima point in the current inclined JICF. In accordance with the streamlines (Fig. 10), this indicates that there is no presence of strong flow reversal in the current inclined JICF. In addition, it is worth noting that the region of the disturbed velocity profile is concentrated, and the enhancement is still observable even at $x/D_o = 5$. Along the vertical velocity profiles, as shown in Fig. 11b, it is interesting to find the presence of two velocity maxima at points C and D at $x/D_o = 3$. The velocity peak at C is due to the deflected jet, while peak D can be attributed to the upwash induced by the CRVP close to the wall. As for VR = 0.75, the time-averaged u and v velocity profiles are shown in Fig. 12. Compared to those at VR = 0.5, the u and v velocity profiles have a larger disturbed region and experience a fast dissipation rate. This is due to the enlarged effective area of jet exit as well as strong mixing between the jet fluid and the crossflow caused by the strong coherent vortices.

The mean jet trajectory describes the extent to which the jet penetrates into the crossflow. However, as the few exiting experimental studies mostly used qualitative visualizations, the trajectory of an inclined jet has not been precisely described. In the current study, the jet trajectories are defined as the streamline originating at the center of the jet orifice extracted from the time-averaged flow fields (Mahesh 2013). As shown in Fig. 13, the trajectories show a clear trend of becoming upright as the VR increases from 0.25 to 1.0. We note that the trajectories at VR = 0.5 and 0.75 are very close. According to the above discussion, this is partly due to reduced effective area of jet exit at VR = 0.5, which results in a higher jet velocity than expectation and, therefore, higher jet trajectory. The different flow structures at VR = 0.5 and VR = 0.75 can also contribute to this close jet trajectories. The periodic formation of the lee-side vortices at VR = 0.75 can entrain the cross-flow fluid into the jet body and enhance the mixing, limiting the penetration heights into the crossflow (New et al. 2006). This finding implies that the effective area of jet exit and flow structures along the jet column should be considered as important parameters when scaling the inclined jet trajectories in further study.

As revealed above, the crossflow has a significant impact on the incline jet. In return, the jet also influences the crossflow. The impact of an inclined JICF on the near-wall region is a crucial consideration in film-cooling applications. To investigate this effect, the time-averaged wall-normal vorticity together with the streamlines and vectors on the wall-parallel plane are presented in Fig. 14. At VR = 0.25 and 0.5 (Fig. 14a, b), a pair of strips with strong vorticity is formed downstream of the exit. According to the streamlines and vectors, this strip pair should be induced by the inwash flow induced by the strong CRVP
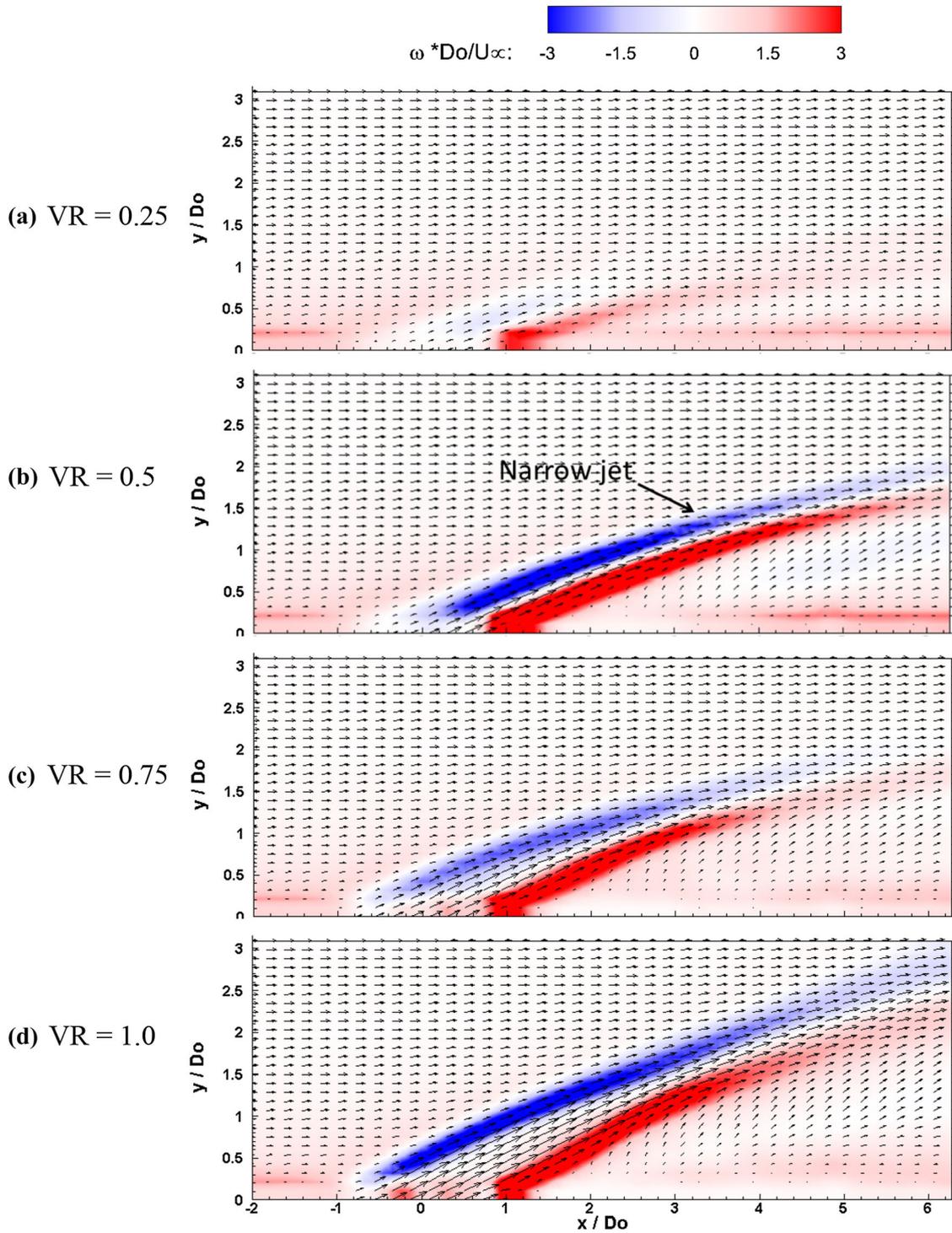
Fig. 6 Contours of time-averaged spanwise vorticity with velocity vectors in the mid-span plane

near the wall. In addition, a pair of strips with opposite-signed vorticity is also observed in the most outboard region. According to the classical normal JICF topology, these outboard vorticity can be induced by the horseshoe vortices originating at the leading edge of the jet exit and developing along with the primary jet vortices. At VR = 0.75 and 1.0 (Fig. 14c, d), it is found that although the jet strength increases, the impact of jets on the near-wall region dissipates fast along the streamwise direction. This is due to their
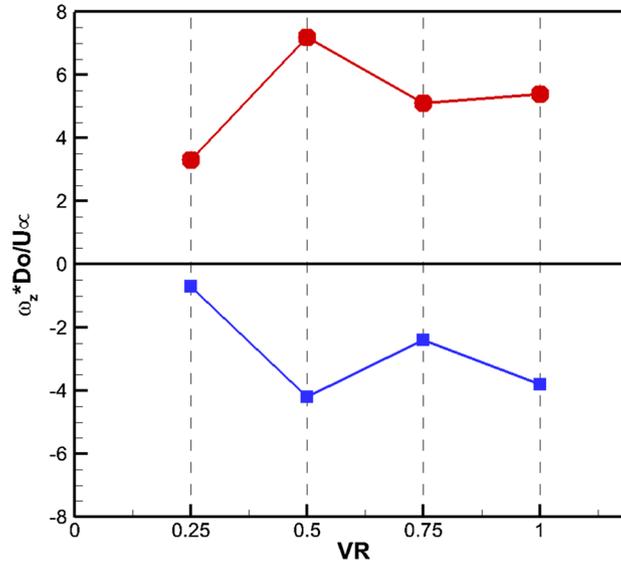
Fig. 7 Peak vorticity on the leading edge (*blue square*) and lee side (*red circle*) of the jet column at different VRs
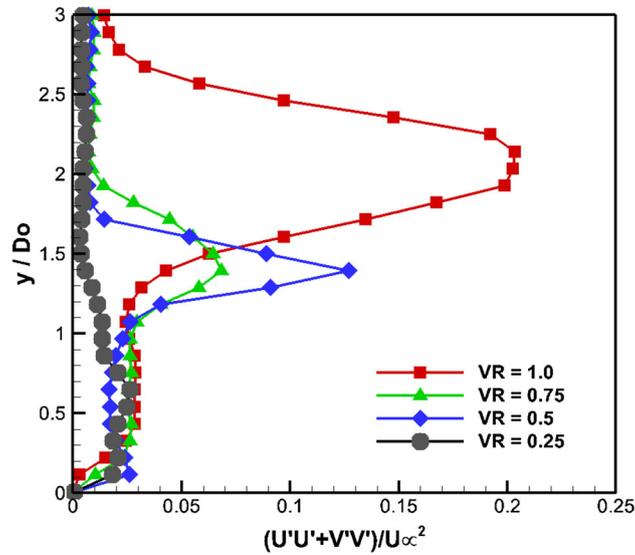
Fig. 8 Turbulent intensity along the line at $x = 5D_o$ on mid-span plane calculated from streamwise and vertical velocity components

long distance from the wall as well as the coherent vortices fast breaking up at far downstream. From the current result, it can be implied that the critical value of VR falls between VR = 0.5 and 0.75 under which the jet can exert strong and effective near-wall impact.

3.4 POD analysis

Numerous studies have demonstrated the effectiveness of POD for detection of energy-carrying, unsteady behavior modes in a complex fluid field (Lumley 1967), including hairpin vortices (Kohli and Bogard 1998), vortex shedding in shear layers (Wen et al. 2016), and free and controlled wake flow (Liu et al. 2014; Ben Chiekh et al. 2013). In POD, a temporal sequence of flow fields consisting of column vectors $u_i(x,t)$ can be written as
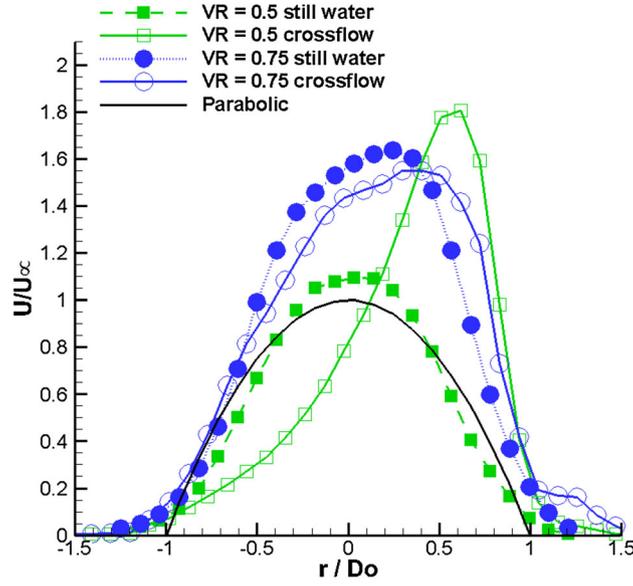
Fig. 9 Speed profiles near to the jet exit extracted from time-averaged flow fields at a location of $y = 0.1D_o$ from the exit at VR = 0.5 and VR = 0.75
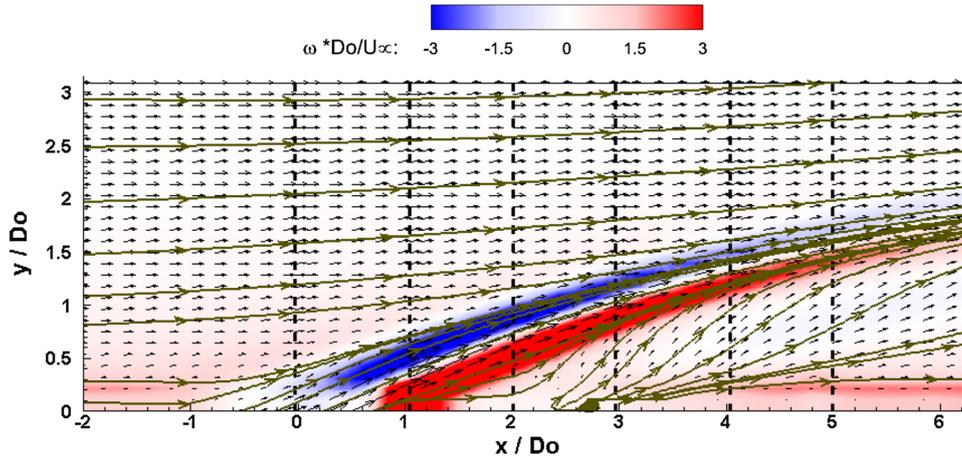
Fig. 10 Contours of time-averaged spanwise vorticity with streamlines and velocity vectors in the mid-span plane at VR = 0.5. *Dashed lines* showing the locations, where the velocity profiles are extracted downstream of the jet exit

$$U = [u_1, \ldots, u_N] \tag{2}$$

where N is the finite number of instantaneous flow fields. Applying the "snapshot" method suggested by Sirovich and Kirby (1987), each instantaneous flow field is treated as a snapshot. The time-dependent velocity field $u(x, t)$ can be decomposed into the form of

$$u(x,t) = \bar{u}(x) + u'(x,t) = \bar{u}(x) + \sum_{n=1}^{N} a_n(t)\phi_n(x) \tag{3}$$

where $\bar{u}(x)$ is the mean velocity field, $u'(x,t)$ is the instantaneous fluctuating velocity field, $\phi_n(x)$ is the spatial POD mode, and $a_n(t)$ is the time-dependent coefficient of the nth POD mode. The POD mode $\phi_n(x)$ is obtained from the eigenvectors A_n of the eigenvalue problem and is ranked according to the size of the eigenvalues λ_n:
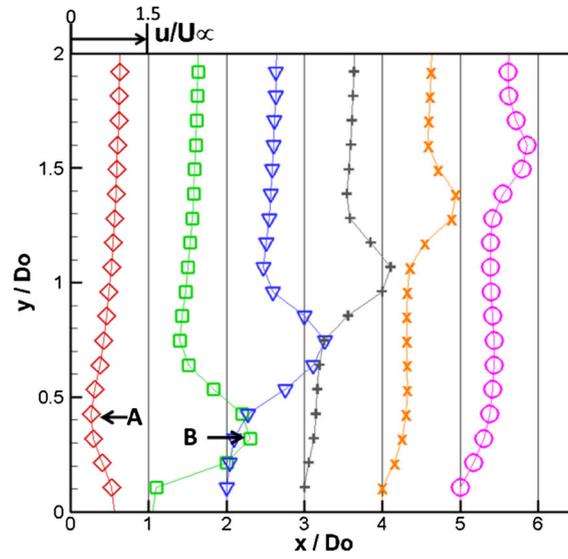
(a) streamwise velocity
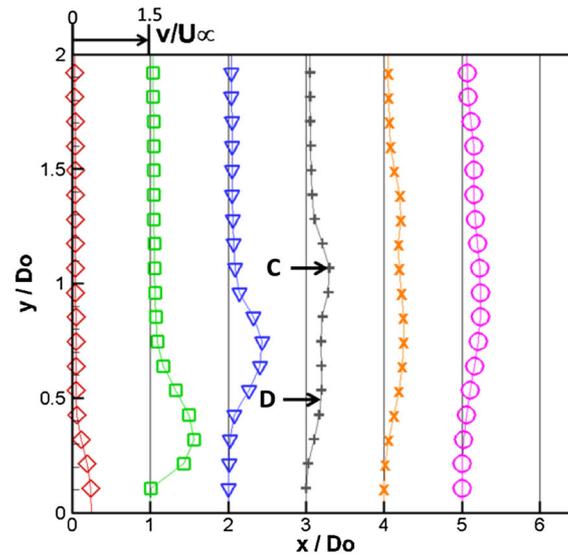
(b) vertical velocity

Fig. 11 Velocity profiles along various downstream locations at VR = 0.5. *Open diamond x = 0, open square x = 1D_o, open triangle x = 2D_o, crosses x = 3D_o, plus symbol x = 4D_o, and open circle x = 5D_o*

$$(U^T U)A_n = \lambda_n A_n. \tag{4}$$

The POD coefficients $a_n(t)$ are determined by projecting the fluctuating part of the velocity field onto the POD modes:

$$a_n(t) = \Psi^T u'(x, t) \tag{5}$$

where $[\Psi = \phi_1(x), \ldots, \phi_N(x)]$ has been introduced. The principle and equations of POD can be found in detail in the literature (Meyer et al. 2007).
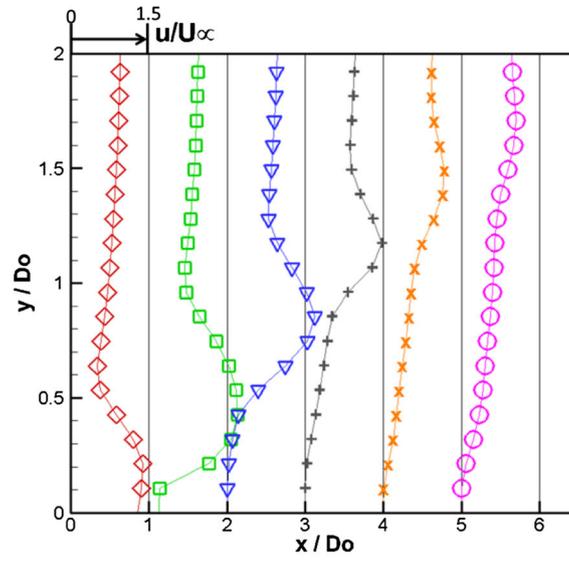
(a) streamwise velocity
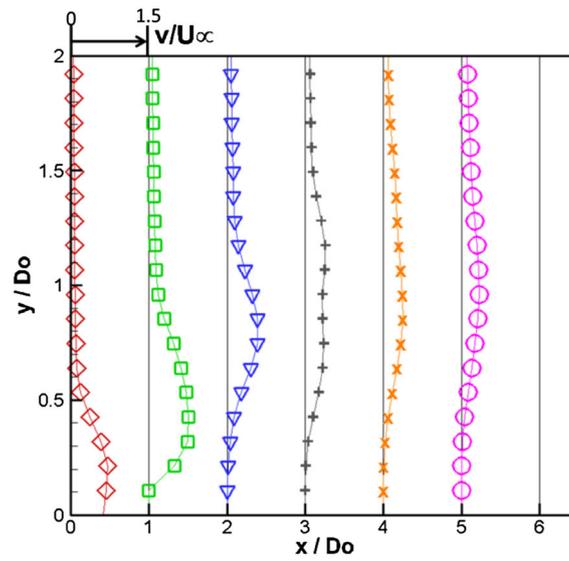
(b) vertical velocity

Fig. 12 Velocity profiles along various downstream locations at VR = 0.75. *Open diamond* $x = 0$, *open square* $x = 1D_o$, *open triangle* $x = 2D_o$, *crosses* $x = 3D_o$, *plus symbol* $x = 4D_o$, and *open circle* $x = 5D_o$
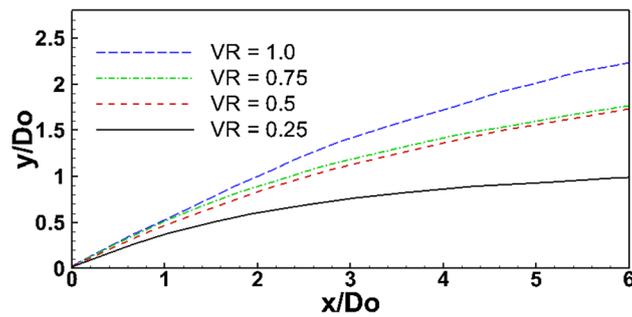
Fig. 13 Trajectories of the inclined jets in crossflow under different VRs
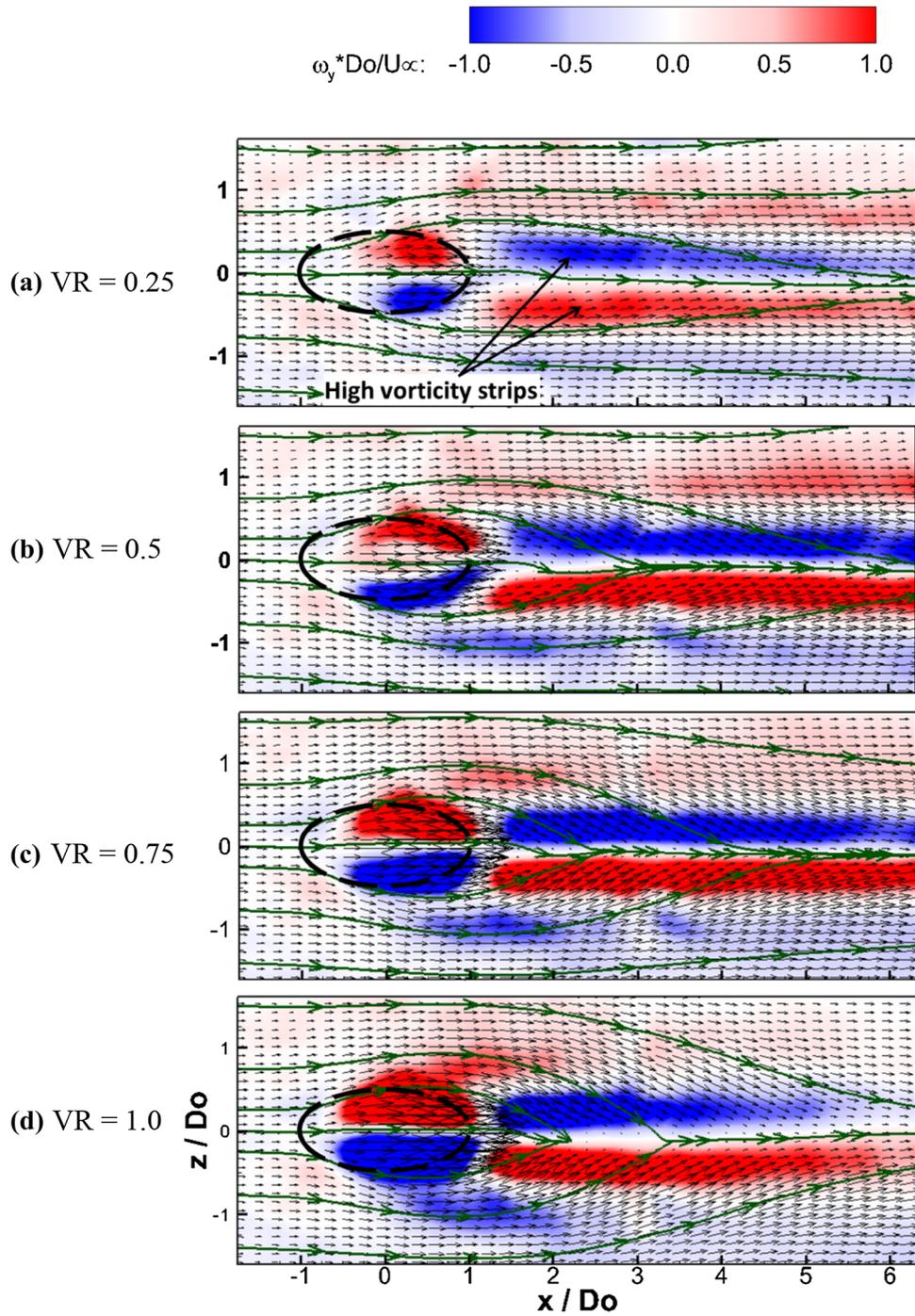
Fig. 14 Contours of time-averaged wall-normal vorticity with velocity vectors and streamlines in the wall-parallel plane

In addition, it is often found that the first POD modes are coupled in pairs between which the flow field oscillates harmonically (Ben Chiekh et al. 2013; Liu et al. 2014; Wen et al. 2016). As such, the POD allows the phase identification of each instantaneous flow field $u(t)$ based on the corresponding coefficients $[\alpha_i(t), \alpha_j(t)]$ of the POD pair (Lengani et al. 2014; Ostermann et al. 2015) as
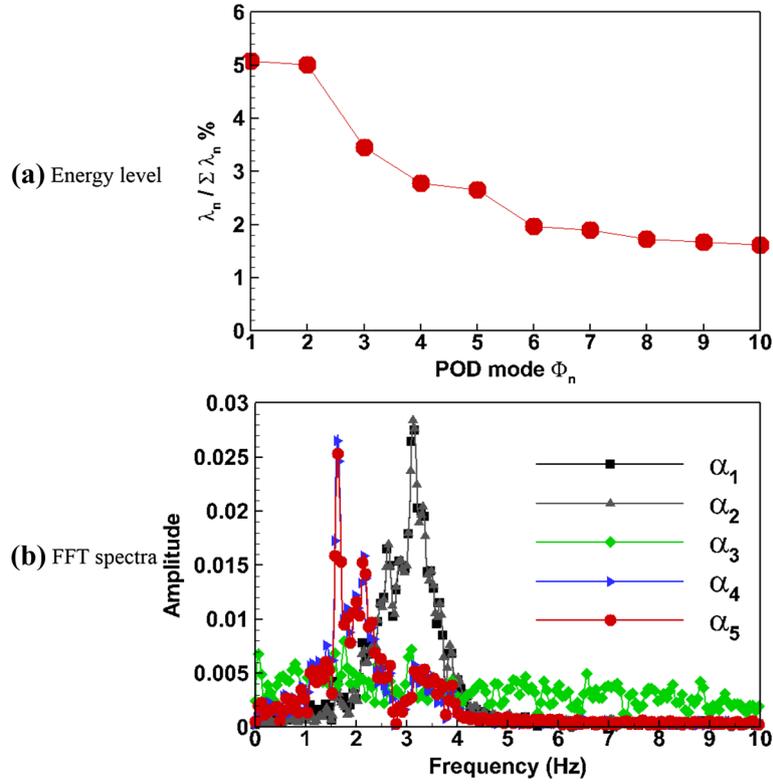
Fig. 15 POD analysis for a VR of 1.0 in the mid-span plane: **a** POD energy levels of the first ten modes and **b** FFT spectra of the first five POD coefficients

$$\beta_{i,j}(t) = \arctan \frac{a_i(t)\lambda_j}{a_j(t)\lambda_i}. \tag{6}$$

Here, the TR-PIV results on the mid-span plane are fed to this POD processing. A convergence study is conducted. It is found that the discrepancy among the first five eigenvalues is within 5% if the number of snapshots is greater than 14,800, which is indeed the case in this study. POD analysis is performed at a sampling frequency of 300 Hz, specially focused on two typical cases: a weakly unsteady flow regime at VR = 0.5 and a highly unsteady flow regime at VR = 1.0. To assess the vortex structures captured in the POD modes, a local swirling strength criterion λ_{ci} is used. At a VR = 0.5, although not shown in the current presentation, the less-unsteady nature of the flow regime is confirmed by the POD analysis. The fluctuation energy of the POD mode is very low. The fast Fourier transform (FFT) analysis of the time-dependent POD coefficients also reveals that the modes are weakly unsteady, because the peaks of fluctuating frequency are very close to zero. In accordance, there is almost no obvious vortex structures captured in the first five most energetic POD modes.

On the other hand, the POD analysis at VR = 1.0 shows obvious unsteady flow patterns and multiple dominating frequencies. As shown by the energetic level in Fig. 15a, the first five modes outstand from the rest. The first two POD modes, Φ_1 and Φ_2, appear as a pair with very close energy levels (5.1 and 5.0%, respectively). They also have very close frequency spectra, which peak at $f \approx 3.1$ Hz, as shown in Fig. 15b. Accordingly, this pair of modes has similar flow structures. As shown in Fig. 16a, b, the flow structures captured by the λ_{ci} criterion in the modes appear alternately along the jet column, with a spatial shift of about 1/4 wavelength. This reveals the convective nature of the flow structures, as widely observed in previous studies (Ben Chiekh et al. 2013; Liu et al. 2014, Wen et al. 2016). Mode Φ_3 shows different behaviors. It has no dominating fluctuation frequency, as shown in Fig. 15b. From the mode field, fluctuating patterns at the leading edge of the jet orifice are captured in Fig. 16c, indicating the unsteady flow induced by the interaction between the emerging jet and the crossflow. Similar to the first two POD modes, the POD modes, Φ_4 and Φ_5, also couple in pair, but with lower energy levels and lower fluctuating
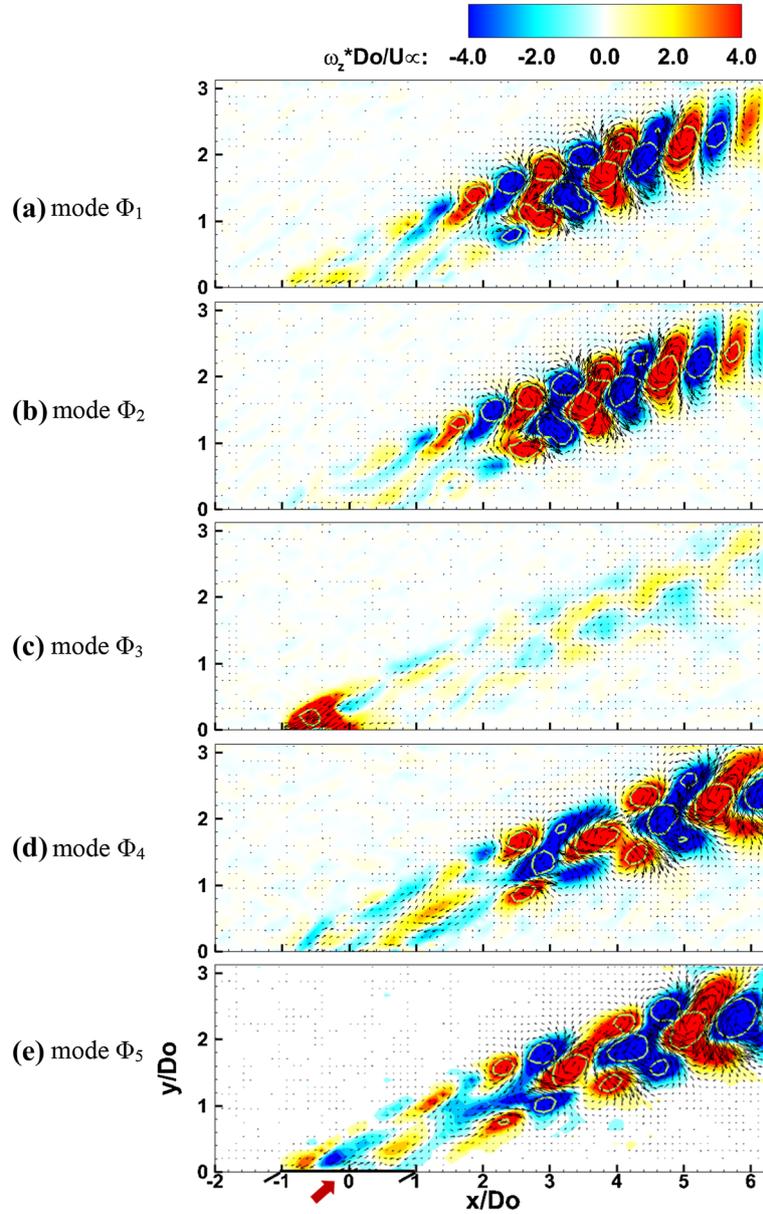
Fig. 16 POD analysis for a VR of 1.0 in the mid-span plane: contours of spanwise vorticity and iso-value of $\lambda_{ci} = 1.5$ (*yellow edge*) with velocity vectors in the first five POD

frequency $f \approx 1.6$ Hz. Accordingly, as shown in Fig. 16d, e, the flow structures in this pair of modes are less coherent and have longer wavelengths.

The two flow patterns captured by the first (Φ_1, Φ_2) and second (Φ_4, Φ_5) POD pairs closely locate along the jet column. To further examine the contribution of these two flow patterns to the highly unsteady flow regime, phase-averaged flow fields are obtained from instantaneous flow fields. Two phase angles, $\beta_{(1, 2)}$ and $\beta_{(4, 5)}$, are calculated based on the corresponding POD coefficients using Eq. 6. To make the fluctuating flow patterns outstanding, the long-time-averaged flow field is subtracted, which is the same in the POD process. The flow field phase-averaged based on $\beta_{(1, 2)}$ is shown in Fig. 17a. According to the instantaneous flow patterns presented above (Fig. 5d), the shedding vortices at the upper row in this phase-averaged flow field are believed to be the weak leading-edge vortices, whereas the lower row the stronger lee-side vortices. On the other hand, the flow field phase-averaged based on $\beta_{(4, 5)}$ only has one row of strong vortices shedding in the jet column, as shown in Fig. 17b. In the case of VR = 0.75, similar flow patterns and corresponding
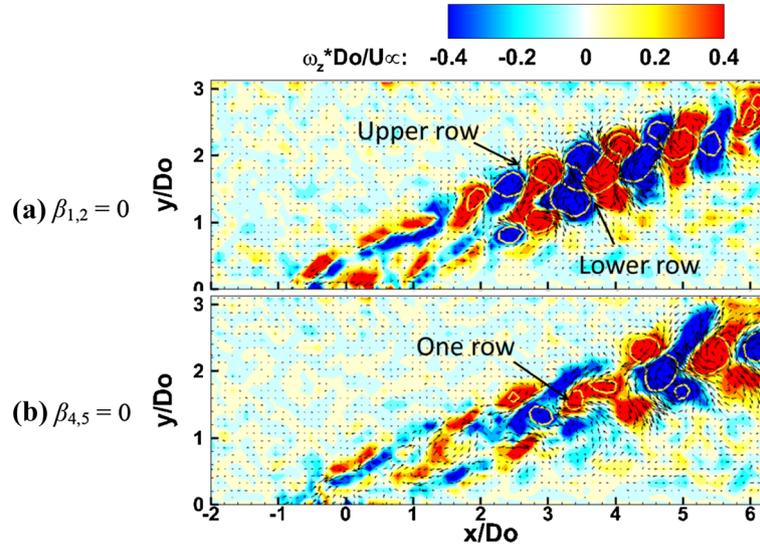
Fig. 17 Phase-averaged flow fields for a VR of 1.0. The phase angle β is calculated based on POD coefficients: **a** $[\alpha_1(t), \alpha_2(t)]$ and **b** $[\alpha_4(t), \alpha_5(t)]$. The long-time-averaged flow field is subtracted

fluctuating frequency ($f \approx 1.3$ Hz) are also extracted from POD mode pair (Φ_5, Φ_6) (not shown here). Therefore, at VR = 1.0, the flow structures extracted by the latter POD pair (Φ_4, Φ_5) are believed to be correspond to the flow field, where only the strong lee-side vortices are obvious. In addition, the phase-averaged flow fields based on the two angles, $\beta_{(1, 2)}$ and $\beta_{(4, 5)}$, show no strong coupling, which is consistent with the fact that the frequencies of the two flow patterns are different. This indicates that the instantaneous flow field at downstream of the jet column is very unstable, varying between the two flow patterns with different fluctuating frequencies. The reason that causes the instability of the flow along the jet column may be due to the unsteady flow near to the exit, where the emerging jet meets the crossflow, as captured by POD mode Φ_3. The detail correlation requires a more thorough study with higher time resolution and a large range of JICF configurations, which, however, is out of the current scope.

4 Conclusions

Experiments were carried out to investigate the near-field interaction of an inclined jet and a crossflow over a flat plate. The details of the flow structures induced at four VRs (0.25, 0.5, 0.75, and 1.0) were visualized and compared using LIF visualization and TR-PIV measurement. The most energetic of the coherent structures in the flow was extracted from the PIV data using POD analysis. The main findings from this study are summarized as follows:

1. It is found that the inclined configuration significantly weakens the interaction between the jet and the crossflow, especially at lower VRs. As such, a weakly unsteady CRVP is formed and barely detaches from the wall in the current inclined configuration at VR ≤0.5 (typically at VR = 0.25), whereas highly unsteady hairpin vortices are well documented to dominate this flow regime in a normal JICF. At higher VRs (typically at VR = 1.0), the inclined JICF fully detaches and corresponds to the beginning of the classical topology of the normal JICF. After careful identification, both CRVP and shear layer vortices are well captured in the current inclined configuration at the higher VRs.
2. The different flow structures and interactions between the inclined jet and the crossflow near the jet exit are found to have strong impact on the distribution of jet-shear layer, the jet trajectory, and the jet influence on the crossflow, especially on the near-wall region. The formation of unsteady shear layer vortices at higher VRs can enhance the mixing between the jet flow and crossflow, resulting in a fast dissipation rate of the jet flow and limiting its penetration. The crossflow has a significant blocking effect on the effective area of the jet exit especially at lower VRs, resulting in a narrow, but high-momentum inclined jet. As such, a strong jet-shear layer and a more upright jet trajectory are induced. In return, the jet also has a strong effect on the near-wall region. However, its influence dissipates

rapidly as VR increases up to 1.0 due to the long penetrating distance in the crossflow and the fast dissipating unsteady flow structures.

3. The POD analysis in the mid-span plane further distinguishes the two different flow regimes. At VR of 1.0, POD reveals that the highly unsteady flow regime is very unstable, varying between two flow patterns with different dominating frequencies, especially at the downstream of the jet column. The first flow pattern is captured by the most energetic POD modes pair, which corresponds to the two rows of the convective leading-edge vortices and the stronger lee-side vortices. The second flow pattern is captured by the latter pair of POD modes, where only one row of the lee-side vortices is obviously induced with a lower dominating frequency. In addition, it also reveals that the jet flow is also remarkably unsteady near to the exit, where the emerging jet meets the crossflow.

References

Acarlar MS, Smith CR (1987) A study of hairpin vortices in a laminar boundary layer. I—Hairpin vortices generated by a hemisphere protuberance. II—Hairpin vortices generated by fluid injection. J Fluid Mech 175(175):1–41

Acharya S, Leedom DH (2012) Large eddy simulations of discrete hole film cooling with plenum inflow orientation effects. J Heat Transf 135(1):011010

Ben Chiekh M, Michard M, Guellouz MS, Béra JC (2013) POD analysis of momentumless trailing edge wake using synthetic jet actuation. Exp Therm Fluid Sci 46:89–102

Bidan G, Nikitopoulos DE (2013) On steady and pulsed low-blowing-ratio transverse jets. J Fluid Mech 714:393–433

Bidan G, Vézier C, Nikitopoulos DE (2012) Study of unforced and modulated film-cooling jets using proper orthogonal decomposition—part I: unforced jets. J Turbomach 135(2):021037

Cambonie T, Aider JL (2014) Transition scenario of the round jet in crossflow topology at low velocity ratios. Phys Fluids 26(8):531–553

Dai C, Jia L, Zhang J, Shu Z, Mi J (2016) On the flow structure of an inclined jet in crossflow at low velocity ratios. Int J Heat Fluid Flow 58:11–18

Fawcett RJ, Wheeler APS, He L, Taylor R (2013) Experimental investigation into the impact of crossflow on the coherent unsteadiness within film cooling flows. Int J Heat Fluid Flow 40:32–42

Foroutan H, Yavuzkurt S (2015) Numerical simulations of the near-field region of film cooling jets under high free stream turbulence: application of RANS and hybrid URANS/large eddy simulation models. J Heat Transf 137(1):011701-011701-12

Fric TF, Roshko A (2006) Vortical structure in the wake of a transverse jet. J Fluid Mech 279:1–47

Guo X, Schröder W, Meinke M (2006) Large-eddy simulations of film cooling flows. Comput Fluids 35(6):587–606

Haven BA, Kurosaka M (1997) Kidney and anti-kidney vortices in crossflow jets. J Fluid Mech 352:27–64

Kalghatgi P, Acharya S (2014) Modal analysis of inclined film cooling jet flow. J Turbomach 136(8):081007

Kelso RM, Smits AJ (1995) Horseshoe vortex systems resulting from the interaction between a laminar boundary layer and a transverse jet. Phys Fluids 7(1):153–158

Kohli A, Bogard DG (1998) Fluctuating thermal field in the near-hole region for film cooling flows. J Turbomach 120(1):86–91

Lengani D, Simoni D, Ubaldi M, Zunino P (2014) POD analysis of the unsteady behavior of a laminar separation bubble. Exp Therm Fluid Sci 58(10):70–79

Lim TT, New TH, Luo SC (2001) On the development of large-scale structures of a jet normal to a cross flow. Phys Fluids 13(3):770–775

Liu Y, Zhang Q (2015) Dynamic mode decomposition of separated flow over a finite blunt plate: time-resolved particle image velocimetry measurements. Exp Fluids 56(7):148

Liu YZ, Shi LL, Yu J (2011) TR-PIV measurement of the wake behind a grooved cylinder at low Reynolds number. J Fluids Struct 27(3):394–407

Liu Y, Zhang Q, Wang S (2014) The identification of coherent structures using proper orthogonal decomposition and dynamic mode decomposition. J Fluids Struct 49(8):53–72

Lumley JL (1967) The structure of inhomogeneous turbulent flow. In: Atmospheric turbulence and radio wave propagation. Nauka, Moscow

Mahesh K (2013) The interaction of jets with crossflow. Annu Rev Fluid Mech 45(1):379–407

Meyer KE, Pedersen JM, Özcan O (2007) A turbulent jet in crossflow analysed with proper orthogonal decomposition. J Fluid Mech 583:199

New TH, Zang B (2015) On the trajectory scaling of tandem twin jets in cross-flow in close proximity. Exp Fluids 56(11):1–12

New TH, Lim TT, Luo SC (2003) Elliptic jets in cross-flow. J Fluid Mech 494(494):119–140

New TH, Lim TT, Luo SC (2006) Effects of jet velocity profiles on a round jet in cross-flow. Exp Fluids 40(6):859–875

Ostermann F, Woszidlo R, Nayeri CN, Christian OP (2015) Phase-averaging methods for the natural flowfield of a fluidic oscillator. AIAA J 53(8):2359–2368

Raffel M, Willert CE, Kompenhans J (2013) Particle image velocimetry: a practical guide. Springer, Berlin

Sakai E, Takahashi T, Watanabe H (2014) Large-eddy simulation of an inclined round jet issuing into a crossflow. Int J Heat Mass Transf 69:300–311

Sau R, Mahesh K (2008) Dynamics and mixing of vortex rings in crossflow. J Fluid Mech 604:389–409

Sinha AK, Bogard DG, Crawford ME (1991) Film-cooling effectiveness downstream of a single row of holes with variable density ratio. J Turbomach 113(3):442

Sirovich L, Kirby M (1987) Low-dimensional procedure for the characterization of human faces. J Opt Soc Am A Opt Image Sci 4(3):519–524

Wen X, Tang H (2014) On hairpin vortices induced by circular synthetic jets in laminar and turbulent boundary layers. Comput Fluids 95:1–18

Wen X, Tang H, Duan F (2015) Vortex dynamics of in-line twin synthetic jets in a laminar boundary layer. Phys Fluids 27(8):083601

Wen X, Tang H, Duan F (2016) Interaction of in-line twin synthetic jets with a separated flow. Phys Fluids 28(4):043602

Willert CE, Gharib M (1991) Digital particle image velocimetry. Exp Fluids 10(4):181–193

Yasuhiko S, Shigeru N, Taketoshi O, Koji O (2000) A highly accurate iterative PIV technique using a gradient method. Meas Sci Technol 11(12):1666

Zhou J, Adrian RJ, Balachandar S, Kendall TM (1999) Mechanisms for generating coherent packets of hairpin vortices in channel flow. J Fluid Mech 387(387):353–396